Demonstration of Receiver-Noise/Distortion Shaping in Antenna Arrays by Using a Spatio-Temporal Δ-Σ Method

Mohammad Radpour, *Member, IEEE*, Zahra Kabirkhoo, *Member, IEEE*, Arjuna Madanayake, *Member, IEEE*, Soumyajit Mandal, *Senior Member, IEEE*, and Leonid Belostotski, *Senior Member, IEEE*

***Abstract*— The spacetime-causality light-cone concept has been well-known since being introduced in Einstein's Special Theory of Relativity, but it has not been explicitly explored in antenna-array electronics. To date, antenna-array radio frequency (RF) receivers have been constructed by replicating RF receiver chains at each array element. Ignoring shared frequency references required for RF-input down-conversion, each receiver in such designs acts independently of its neighbors until the received signals reach the array beamformer. While the use of independent receiver chains is convenient, it is not the optimum and does not take advantage of the additional opportunities afforded by the light-cone concept. This work presents the first experimental demonstration of noise and distortion (ND) shaping. The NDs originating in the receiver itself are spatio-temporally shaped away from the beamformer region of support (ROS), thereby permitting their suppression by the beamformer. The demonstrator is a 24.3–28.7-GHz 79.28-mW 4-port receiver for a 4-element linear antenna array implemented in 22-nm FDSOI CMOS. When shaping was enabled, the demonstrator provided average improvements to the noise figure (NF) of 1.6 dB, IP1dB of 2.25 dB, and IIP3 of 1.4 dB (compared to a reference design), and achieved NF = 2.6 dB, IP1dB = −18.7 dBm, and IIP3 = −12.5 dBm while consuming 19.8 mW/ch.**

***Index Terms*— Antenna array, delta-sigma modulator, multi-port receiver, spatio-temporal (ST) noise shaping.**

I. Introduction

ANTENNA arrays provide significant growth opportunities in the wireless industry, as well as in the development of radar and imaging systems [1]. However, antenna arrays pose various engineering challenges. For example, they must be able to generate sharp, steerable beams to mitigate free-space path loss in high-frequency communication networks [2]. While such beams are critical for closing communication links, the implementation of N-element-array electronics increases circuit complexity. This increased complexity necessitates the use of receivers (Rxs) that are capable of providing efficient resource usage, while still achieving the anticipated performance advantages. The conventional approach to designing N-element arrays [3], [4], [5] is based on replicating RF receivers at each element. In such designs, apart from shared frequency references, each receiver chain acts independently of its neighbor [6], with the only connection being through the beamformer in order to create beams. Although the use of independent receiver chains is convenient, it is suboptimal because it ignores the relationships between the signals and receiver noise and distortion (ND) across the array [7]. As a result, the receiver's NDs fall within the beamformer beam, which is configured to retain a certain portion of the spatio-temporal (ST) spectrum in order to receive information from a particular direction and over a specific frequency bandwidth.

In this work, the Rx chains are interconnected by modifying conventional temporal Δ-Σ-modulator theory [8]. The Δ-Σ method is often used in analog-to-digital converters (ADCs) in conjunction with temporal oversampling to shape the nonlinearity of a coarse quantizer away from the temporal bandwidths of circuits. Since analog-array receivers do not include samplers until beamforming or after it, they cannot make use of temporal oversampling. However, *spatial sampling is present in all arrays due to the discrete locations of antennas*. Therefore, arrays can employ oversampling in the spatial domain by placing antennas closer than half a wavelength apart and enlarging the area outside the light cone (see Section II-D), denoted as the "Elsewhere" region and is also known as "the cone of silence" [9], which is the region that can never be occupied by propagating EM waves. This concept was theorized by us in [10] where simulations of a 4-GHz network showed noise shaping for oversampling factors of 2 and 4. Unfortunately, this strategy requires an increase in the number of antennas, which is undesirable for cost-sensitive networks. Instead of oversampling, this work exploits the sparsity of the frequency-domain plane-wave (PW) region of support (ROS) to eliminate undesired receiver NDs and reports on the resultant ND shaping-receiver (sRx) demonstrator.

Manuscript received 20 November 2023; revised 13 January 2024; accepted 26 January 2024. Date of publication 13 February 2024; date of current version 7 August 2024. This work was supported in part by Natural Sciences and Engineering Research Council (NSERC) Discovery under Grant RGPIN/03855-2018; in part by NSERC Discovery Accelerator under Grant RGPAS/522621-2018; in part by NSERC Research Tools and Instruments Program under Grant RTI/00075-2021; in part by the Canada Research Chair Program under Grant 231990; and in part by the U.S. National Science Foundation (NSF): SpecEES: Collaborative Research: Spatially Oversampled Dense Multi-Beam Millimeter-Wave Communications for Exponentially Increased Energy-Efficiency under Award 1854798. *(Corresponding author: Leonid Belostotski.)*

Mohammad Radpour, Zahra Kabirkhoo, and Leonid Belostotski are with the Department of Electrical and Software Engineering, University of Calgary, Calgary, AB T2N 1N4, Canada (e-mail: mohammad.radpour1@ucalgary.ca; zahra.kabirkhoo@ucalgary.ca; lbelosto@ucalgary.ca).

Arjuna Madanayake is with the Department of Electrical and Computer Engineering, Florida International University, Miami, FL 32611 USA (e-mail: amadanay@fiu.edu).

Soumyajit Mandal is with the Instrumentation Division, Brookhaven National Laboratory, Upton, NY 11973 USA.

Color versions of one or more figures in this article are available at https://doi.org/10.1109/TMTT.2024.3360192.

Digital Object Identifier 10.1109/TMTT.2024.3360192

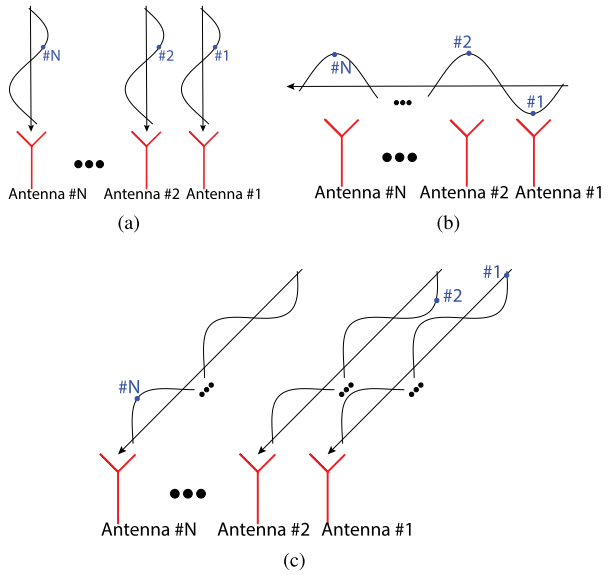

Fig. 1. Spatial sampling with antenna arrays. Sampling at a certain moment in time is identified with dots and the associated antenna numbers. (a) Plane wave at boresight. (b) Plane wave at endfire. (c) Plane wave at arriving at an angle between 0° and 90°.

In this demonstrator, the Rx chains are not independent of each other, which allows the propagation of the undesired NDs from each chain to its neighbors, thereby placing them in the "Elsewhere" region. When in the "Elsewhere" region, NDs are outside the beamwidth of the subsequent beamformer, and therefore, are filtered out by it.

Section II of this article provides a review of the background information relating to spatial sampling as well as the PWs and their ROSs on multidimensional frequency planes, while the ST ND shaping is introduced in Section III. The proposed circuits and the measurement results are presented in Sections IV and V. Finally, Section VI concludes this article.

II. Background

A. Spatial Sampling

Sampling analog waveforms in the time domain (i.e., temporal sampling) is a well-known concept employed widely in devices such as ADCs and sample-and-hold circuits. These devices rely on a timing signal, commonly known as "clock," to provide accurate timing references, guaranteeing that each sample is taken at regular time intervals.

However, sampling can extend beyond the time domain. In this work, we make use of spatial sampling. As spatial sampling is not yet as common in the microwave community as the temporal sampling, it is instructive to review it here and give some insight into the concept. Readers are encouraged to review [11], [12], [13], [14], [15], [16], [17], [18] for additional examples of applying spatial sampling to realize beamformers.

Whereas the temporal sampling is the conversion of a continuous-time signal into a discrete signal via taking samples at specific time intervals, spatial sampling is the conversion of a continuous signal into discrete signals by sensors located at specific spatial intervals. A relevant example of such sensors would be antennas in an array.

Fig. 1 helps illustrate this concept. We start by considering a PW reaching antenna array at boresight in Fig. 1(a). At the same instance in time, all N antennas sample the same voltage. This is analogous to a temporal sampling of a dc voltage, when at every sampling moment the input signal is constant, i.e., 0 rad/s. Analogously, for the spatial sampling, the boresight incidence corresponds to a 0 rad/m frequency. As the incidence angle increases from 0°, the voltages detected by each antenna become different due to the delay experienced by the PW as it reaches the array antennas. At the extreme, the direction of arrival (DOA) is endfire as in Fig. 1(b). In this case, for an array with half-wavelength antenna spacing receiving a sine-wave signal, the voltage samples received by antennas are 180° out of phase, which is equivalent to having two samples per period, i.e., the Nyquist sampling criterion. When the DOA falls between boresight and endfire, Fig. 1(c) identifies parts of the waveform that are seen by the antennas at a certain moment in time. As shown, the antennas sense different parts of the PW. In terms of the more-familiar temporal sampling, this situation is equivalent to having the sampled signal vary with time. Therefore, this DOA exhibit spatial frequency higher than 0 rad/m.

B. Spatial-Frequency Domain

The conversion of a signal $s(t)$ acquired in the temporal domain to its temporal-frequency-domain representation $S(\omega_t)$ is done via the Fourier transform

$$S(\omega_t) = \int_{-\infty}^{\infty} s(t) e^{-j(\omega_t t)} \mathrm{d}t \tag{1}$$

where ω_t is the temporal angular frequency. RF and microwave filters, e.g., bandpass filters, are typically designed in the temporal-frequency domain to pass some desired frequencies and attenuate others that fall outside the passband of these filters.

Similarly, a signal $s(x)$ acquired in the spatial domain can be represented in the spatial-frequency domain by using the Fourier transform

$$S(\omega_x) = \int_{-\infty}^{\infty} s(x) e^{-j(\omega_x x)} \mathrm{d}x \tag{2}$$

where ω_x is the spatial angular frequency. $S(\omega_x)$ describes the spatial frequencies present in the signal $s(x)$, and, in the context of this work, these frequencies are related to the DOA of a PW to an antenna array. Filtering in the spatial-frequency domain permits certain frequencies to pass through a filter passband while blocking other spatial frequencies. Since spatial frequencies relate to the DOA of a PW, spatial filtering is responsible for passing signals from the DOAs within its spatial passband and rejecting frequencies outside the passband. This type of filtering is often called "beamforming."

C. ROS of a Plane Wave

To investigate the ROSs of the PWs, we begin by considering an EM wave propagating in a 4-D space $w_{\mathrm{PW}}(x, y, z, ct)$, where $(x, y, z) \in \mathbb{R}^3$ are the 3-D spatial dimensions, $t \in \mathbb{R}$ is the time, and c is the speed of the EM wave. The DOA of the EM wave arriving at a 3-D antenna array at an azimuth angle θ_a and the elevation angle θ_e is given by a vector $\hat{\boldsymbol{\omega}} = [\hat{\omega}_x, \hat{\omega}_y, \hat{\omega}_z]$, where $\hat{\omega}_x = (\omega/c)\cos(\theta_a)\sin(\theta_e)$, $\hat{\omega}_y = (\omega/c)\sin(\theta_a)\sin(\theta_e)$, and $\hat{\omega}_z = (\omega/c)\cos(\theta_e)$, $\hat{\omega}_x$ and $\hat{\omega}_y$ are transverse coordinates and

$\hat{\omega}_z$ is the longitudinal coordinate of the wave vector along the x-, y-, z-axes in the spatial-frequency domain $\boldsymbol{\omega} = [\omega_x, \omega_y, \omega_z]$ [19], [20, ch. 2]. This propagating wave can be described as

$$w_{PW} = w_0 e^{j(\hat{\boldsymbol{\omega}} \cdot \boldsymbol{r} + \omega_t t)} \tag{3}$$

where $\boldsymbol{r} = [x, y, z]$ is a point in space. In antenna arrays, w_{PW} in (3) represents a far-field PW with a spatial DOA of (θ_a, θ_e) that reaches the antenna array at time t.

A vast majority of arrays are either linear arrays or planar arrays located at $z = 0$ plane. In this case, the 3-D Fourier transform of w_{PW} determines $W_{PW}(\boldsymbol{\omega})$, where $\boldsymbol{\omega} = [\omega_x, \omega_y, \omega_t]$, via

$$W_{PW} = \iint_{R^2} \int_{t=-\infty}^{\infty} w_{PW}(x, y, ct) e^{-j(\boldsymbol{\omega} \cdot \boldsymbol{r} + \omega_t t)} \mathrm{d}t \mathrm{d}^2\boldsymbol{r}. \tag{4}$$

The integrals in (4) can be separated; therefore, the Fourier transform of a PW gives

$$\begin{aligned} W_{PW}(\omega) &= \iint_{R^2} x_{PW}(x, y) e^{-j\boldsymbol{\omega} \cdot \boldsymbol{r}} \mathrm{d}^2\boldsymbol{r} \times \int_{-\infty}^{\infty} x_{PW}(t) e^{-j(\omega_t t)} \mathrm{d}t \\ &= (2\pi)^2 \delta(\omega_x - \hat{\omega}_x) \delta(\omega_y - \hat{\omega}_y) X_{PW}(\omega_t). \end{aligned} \tag{5}$$

The Dirac terms, $\delta(\cdot)$, imply that the ROS of a PW in the 3-D ST frequency domain *lies along a line* passing through the origin [11], [21]. This line occupies a small portion of the 3-D ST frequency space. Similarly, for a 1-D linear array, ROSs occupy the small portions of the 2-D ST frequency space. This *sparsity of the ROS in the ST frequency domains* is exploited in this work.

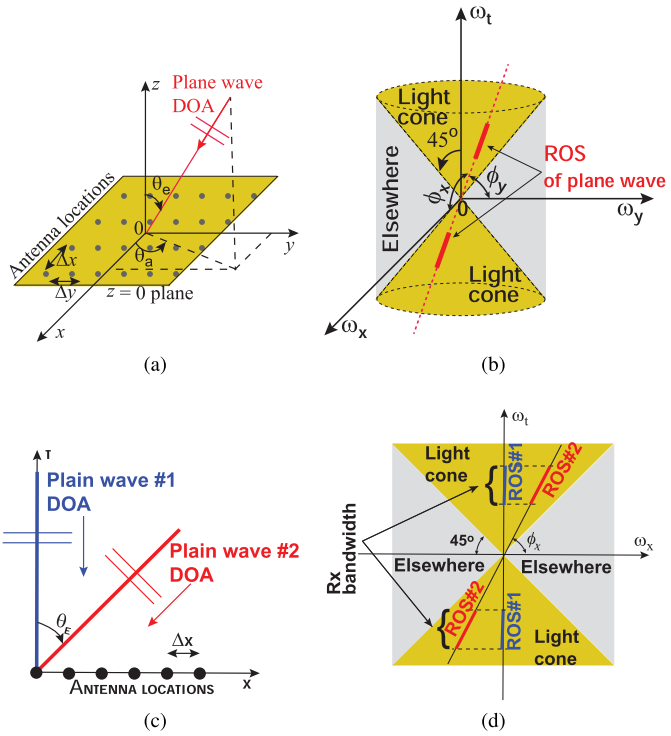

Fig. 2. (a) DOAs of a PW to a planar array located at $z = 0$ and (b) ROS of that PW within the "light cone". (c) DOAs of two PWs arriving to a linear uniformly spaced array and (d) their ROSs within the "light cone". Uniform antenna spacing is assumed at half wavelength of the upper temporal frequency of a band-limited receiver. ω_t and $\omega_{x,y}$ are the temporal and spatial angular frequencies.

D. Light Cone

If we further consider the x direction of a 2-D planar array and describe (3) by its periodic characteristic as $w_{PW}(x, ct) = w_{PW}(x\cos(\theta_e) + ct)$. The relationship between θ_e and the ROS angle ϕ_x is

$$\phi_x = \arctan(\sin(\theta_e)) \tag{6}$$

where $-(\pi/2) \leq \theta_e \leq (\pi/2)$. Given the angular relationship in (6), the limits of the spatial DOA can be mapped to the ST domain "light cone" as

$$-\frac{\pi}{4} \leq \phi_x \leq \frac{\pi}{4}. \tag{7}$$

Similarly for the y direction, the ROS angle ϕ_y is

$$-\frac{\pi}{4} \leq \phi_y \leq \frac{\pi}{4}. \tag{8}$$

A PW, having a certain DOA, can be represented in a temporal and spatial 3-D and 2-D planes as illustrated in Figs. 2(a) and (c) for a 2-D planar array and a 1-D linear array, respectively. A Fourier transform can then be used to describe the ST frequency response of the PWs. These frequency responses are the aforementioned ROSs and are illustrated in Fig. 2(b) and (d), which represent more complete versions of what is shown in Fig. 1. The ROSs in Fig. 2(b) and (d) illustrate the 3-D and 2-D frequency spectra of PWs in Fig. 2(a) and (c), respectively, and show the geometrical representation of (5), wherein the ROS for a PW is a straight line that passes through the origin and lies within the light cone (yellow area).

In a conventional array receiver, a spatial filter (i.e., a beamformer) with a certain bandwidth directionally enhances a temporally band-limited portion of the desired ROS and spatio-temporally filters out other signals, even though they may have the same temporal frequencies as the desired signals. Any signals located in the regions away (in the spatial-frequency sense) from the desired ROS are removed by the beamformer, including anything outside the "light cone" [i.e., in the "Elsewhere" regions in Fig. 2(b) and (d) that can never be occupied by a propagating PW].

Based on this analysis, it follows that networks that place *receiver-introduced* NDs outside the "light cone" or away from the sparse ROS can achieve the clean removal of unwanted NDs using *any conventional beamformer*, thus making them suitable for use in the majority of antenna-array receiver systems.

III. ST ND Shaping

A. Noise-and-Distortion Shaping

Δ-Σ modulation is often used in ADCs to reduce the nonlinearity of low-precision quantizers. A block diagram of such Δ-Σ ADC is shown in Fig. 3(a).

Δ-Σ methods are not limited to ADCs, and the source of non-linearity mitigated by such systems is not necessarily a quantizer. A block diagram of an sRx, a Δ-Σ modulator for shaping NDs in antenna arrays, is shown in Fig. 3(b), where the integrator is represented by a 3-D ST integrator, $I(\boldsymbol{s})$ where $\boldsymbol{s} = (s_x, s_y, s_t)$, and the receiver is represented

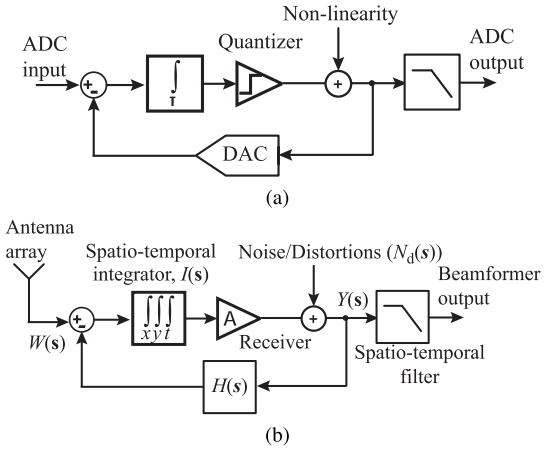

Fig. 3. (a) Δ-Σ ADC block diagram, where a digital-to-analog converter (DAC) provides a feedback path. (b) Block diagram of an sRx based on the Δ-Σ method for ND shaping.

by its gain A and its noise and distortions $N_d(\boldsymbol{s})$. In this representation, $s_{x,y} = j\omega_{x,y}$ and $s_t = j\omega_t$ are the spatial and temporal (i.e., conventionally used) Laplace variables, $W(\boldsymbol{s}) \overset{\mathscr{L}}{\leftrightarrow} w(x, y, t)$ is the input to the sRx in the continuous ST Laplace domain, $N_d(\boldsymbol{s}) \overset{\mathscr{L}}{\leftrightarrow} n_d(x, y, t)$ denotes the receiver's ND in the ST Laplace domain at the receiver output, $Y(\boldsymbol{s}) \overset{\mathscr{L}}{\leftrightarrow} y(x, y, t)$ is the network output, and $H(\boldsymbol{s}) \overset{\mathscr{L}}{\leftrightarrow} h(x, y, t)$ is the feedback transfer function.

As we have not yet discretized either space or time dimensions, the space and time are, therefore, continuous domains and represent electromagnetic phenomena in the space-time continuum, where radio wave propagation occurs through linear electromagnetics, as described by Maxwell's equations.

We express the output signal as

$$Y(\boldsymbol{s}) = A \times E(\boldsymbol{s})I(\boldsymbol{s}) + N_d(\boldsymbol{s}) \tag{9}$$

where $E(\boldsymbol{s}) = W(\boldsymbol{s}) - H(\boldsymbol{s})Y(\boldsymbol{s})$. Using the 3-D beamfilter realization via passband slices in [22] and [11], a 3-D ideal integrator is written as

$$I(\boldsymbol{s}) = \frac{1}{T_x \sin(\phi_x)s_x + T_t \cos(\phi_x)s_t} \times \frac{1}{T_y \sin(\phi_y)s_y + T_t \cos(\phi_y)s_t} \tag{10}$$

where angles $\phi_{x,y}$ identify the orientation of the integrator ROS in the first quadrant of the 3-D domain. The ST integrator $I(\boldsymbol{s})$ has the "bandwidth constants" $T_{x,y,t}$, which are the main visual difference between the conventional Δ-Σ modulator that only has a temporal integrator and the Δ-Σ network discussed here. The ST integrator $I(\boldsymbol{s})$ shapes NDs in 3-D and is suitable for all ROSs within the light cone. For a linear array of antennas, (10) reduces to

$$I(s_x, s_t) = \frac{1}{T_x \sin(\phi_x)s_x + T_t \cos(\phi_x)s_t}. \tag{11}$$

Plugging in the expression for $E(\boldsymbol{s})$ in (9) gives the 3-D input-output relationship

$$[1 + A \times H(\boldsymbol{s})I(\boldsymbol{s})]Y(\boldsymbol{s}) = A \times I(\boldsymbol{s})W(\boldsymbol{s}) + N_d(\boldsymbol{s}). \tag{12}$$

Simplifying the result produces

$$Y(\boldsymbol{s}) = W(\boldsymbol{s})\frac{A \times I(\boldsymbol{s})}{1 + A\beta \times I(\boldsymbol{s})} + N_d(\boldsymbol{s})\frac{1}{1 + A\beta \times I(\boldsymbol{s})} \tag{13}$$

where A is the receiver voltage gain and the attenuator, $\beta = 1/A$, is used instead of $H(\boldsymbol{s})$ to ensure that βY and W are of the same magnitude so that E is not dominated by either of them.

B. Linear-Array System Concept

In this work, a linear uniformly spaced array is considered. Fig. 4 illustrates the evolution of the proposed noise-shaping concept. This concept originates with a typical RF receiver, where all of its NDs are shown explicitly as "Rx noise/distortion." We can apply the Δ-Σ method to this receiver as illustrated to shape these NDs outside the passband of a lowpass filter. However, this requires having temporal oversampling built into the network. Taking this concept further, as in Fig. 3(b), and using spatial (over)sampling leads us to the proposed array system in Fig. 4. In this system, the 2-D frequency spectra at the array input and at the input to the beamformer are shown to illustrate the ST locations of NDs contributed by different parts of the array. The beamformer, i.e., the spatial filter, passes only the desired signal and filters out noise that is placed away from its ST passband.

C. ND-Shaping Demonstrator Implementation Details

To realize a network that can place NDs outside the "light cone" or away from the ROS, we start with an initial block diagram of an ND-shaping sRx based on a conventional temporal Δ-Σ circuit in Fig. 3(a) but implemented in the spatial domain [Fig. 5(a)], where an LNA replaces the Rx in Fig. 4.

We rewrite (13) for a 2-D case associated with a linear antenna array as

$$Y(s_x, s_t) = \frac{AW(s_x, s_t)}{A\beta + T_x s_x} + N_d(s_x, s_t)\frac{T_x s_x}{A\beta + T_x s_x} \tag{14}$$

where $I(s_x, s_t)$ in (11) is simplified to $I(s_x) = 1/T_x s_x$ for a PW at boresight.

In Fig. 5(a), the desired signals and NDs are both 2-D signals in the ST domain. The spatial-integrator block, $I(s_x)$, has the "bandwidth constant" of T_x, and takes place of the temporal integrator in the conventional Δ-Σ block diagram, as in Fig. 3(a). An ST integrator $I(s_x, s_t)$ in (11) would shape NDs in 2-D thus making ND shaping apply to ROSs near the light cone edges. However, in the sRx demonstrator described in this work, only a spatial integrator $I(s_x)$ is used. An examination of (14) shows that the input signal (W) is lowpass filtered in the spatial domain, while the NDs are highpass filtered. That is, the NDs are spatio-temporally shaped away from overlap with the desired signal for subsequent removal by a spatial filter/beamformer.

In practice, the system in Fig. 5(a) is unrealizable because antenna elements are not a continuous structure; rather, they are located at spacings Δx. Given that electromagnetic waves are measured in space-time using arrays of antennas, we discretize the spatial variable such that $x = i\Delta x$, where i is

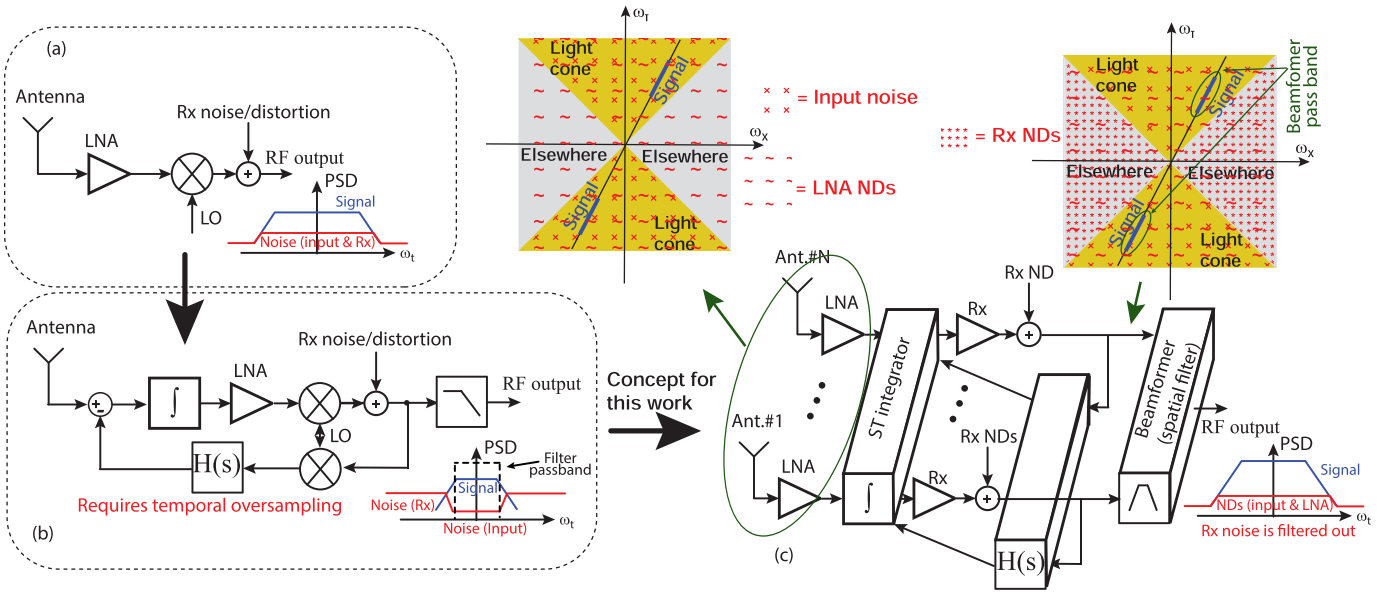

Fig. 4. Conceptual idea explored in this work. It starts with a conventional receiver in (a) that introduces noise and distortions to the received signal. This circuit evolves to (b) by introducing noise shaping that requires an integrator, a feedback network, and a filter. This is then extended to (c), which shows an N-antenna ND-shaping network that is investigated in this work. (a)–(c) Corresponding noise power-spectral densities (PSDs) for the receivers are shown with PSD plots. Two ST frequency plots show ST locations of noise at the N-antenna LNA outputs and at the inputs to be beamformer in (c).

an index for position. This yields the continuous-time signal triplets, $w(i,t)$, $y(i,t)$, and $n_{\rm d}(i,t)$, which correspond with the temporal Laplace transforms, $W(i,s_{\rm t})$, $Y(i,s_{\rm t})$, and $N_{\rm d}(i,s_{\rm t})$, respectively. Next, it is necessary to derive a difference equation that implements the desired noise-shaping operation as an iterative algorithm that forms a multi-dimensional filter. To make the Δ-Σ system in Fig. 5(a) realizable, we use an Euler transform, which, in the complex z domain, is $T_{\rm x}s_{\rm x} = A\beta(1-z_{\rm x}^{-1})/z_{\rm x}^{-1}$, to discretize the system in the spatial domain and obtain

$$Y(z_{\rm x},s_{\rm t}) = \frac{W(z_{\rm x},s_{\rm t})z_{\rm x}^{-1}}{\beta} + N_{\rm d}(z_{\rm x},s_{\rm t})\big(1-z_{\rm x}^{-1}\big). \tag{15}$$

By selecting $\beta = 1/A$ yields the output in its noise-shaped form, with the forward gain remaining unchanged as $Y(z_{\rm x},s_{\rm t}) = AW(z_{\rm x},s_{\rm t})z_{\rm x}^{-1} + N_{\rm d}(z_{\rm x},s_{\rm t})(1-z_{\rm x}^{-1})$. Furthermore, signals flowing through the $z_{\rm x}^{-1}$ blocks can be obtained by connecting receiver chains to their neighbors, thereby introducing signal flow between the receiver chains. Without incurring a loss of generality, the output can be rewritten as

$$Y(z_{\rm x},s_{\rm t}) = A\times W(z_{\rm x},s_{\rm t}) + \big(1-z_{\rm x}^{-1}\big)N_{\rm d}(z_{\rm x},s_{\rm t}). \tag{16}$$

In the 2-D frequency domain, the independent frequency variables, $\omega_{\rm x}$ and $\omega_{\rm t}$, drive the transform variables via $z_{\rm x} = e^{j\omega_{\rm x}}$ and $s_{\rm t} = j\omega_{\rm t}$, respectively. The shaped noise transfer function in the 2-D frequency domain $(\omega_{\rm x},\omega_{\rm t}) \in \mathbb{R}^2$ is therefore given by the complex function $1-e^{-j\omega_{\rm x}}$. At temporal frequency $\omega_{\rm t}$, the corresponding spatial frequency for a propagating planar wave is $\omega_{\rm x} = (\omega_{\rm t}/c)\sin(\theta_{\rm e})$, where $\theta_{\rm e}$ is the DOA and $-\pi/2 \le \theta_{\rm e} < \pi/2$. An infinite-impulse-response implementation of (16) is shown in Fig. 5(b), where the input, $W(z_{\rm x},s_{\rm t})$, is amplified and the ND is shaped by the spatial highpass filter $(1-z_{\rm x}^{-1})$. The block identified as the "spatial integrator" creates the error signal $E_{\rm i}$ by subtracting an attenuated output of the previous LNA ($Y_{\rm i\text{-}1}$) from the signal generated by the previous antenna ($W_{\rm i\text{-}1}$). The delay stage τ_d compensates the LNA group delay by delaying $W_{\rm i\text{-}1}$ prior to subtraction. This results in $E_{\rm i} = W_{\rm i\text{-}1} - \beta Y_{\rm i\text{-}1} \approx -N_{\rm d,i\text{-}1}$, where $N_{\rm d,i\text{-}1}$ is the ND generated in the adjacent chain. Adding this to the signal at the local antenna ($W_{\rm i}$) and feeding the result into the LNA produces

$$Y_{\rm i} \approx AW_{\rm i} + \big(N_{\rm d,i} - N_{\rm d,i\text{-}1}\big). \tag{17}$$

This shows that the input signal is amplified whereas NDs are highpass filtered.

Using the circuit in Fig. 5(b) results in a novel sRx that can be implemented as shown in Fig. 5(c), where the red lines identify connections between the chains. Each chain i in Fig. 5(c) is formed adding two inputs ($w_{\rm i}$ and $w_{\rm i\text{-}1}$) to the outputs of an adjacent chain ($y_{\rm i\text{-}1}$) and its spatial integrator ($p_{\rm i\text{-}1}$).

As in any array, the desired incoming signals experience phase shifts based on the antenna spacing Δx and the DOA. The maximum phase shift of 180° is for signals at the maximum temporal frequency with the DOA at endfire and half-wavelength antenna spacing. Unlike the desired signals, the NDs in the system in Fig. 5(a) exhibit phase shifts from one receiver to the next that are independent of the incoming-signal DOA. Thus, NDs can exhibit $\ge$ 180° phase shift, regardless of the antenna spacing and the DOA of the desired signal. This is equivalent to having an apparently different speed of propagation for the unwanted NDs and pushes them away from the ROS and into the "Elsewhere" region. Fig. 6(a) demonstrates numerical simulations of the 2-D noise shaping of (16) with a 128-element linear array. As can be seen, the noise is shaped toward $\omega_{\rm x} = \pm\pi$ and away from $\omega_{\rm x} = 0$ as desired.

The circuit in Fig. 5(b) requires an adder for $P_{\rm i\text{-}1}(z_{\rm x},s_{\rm t})$ at the input to the LNA. As the adder output ($P_{\rm i}$) has to

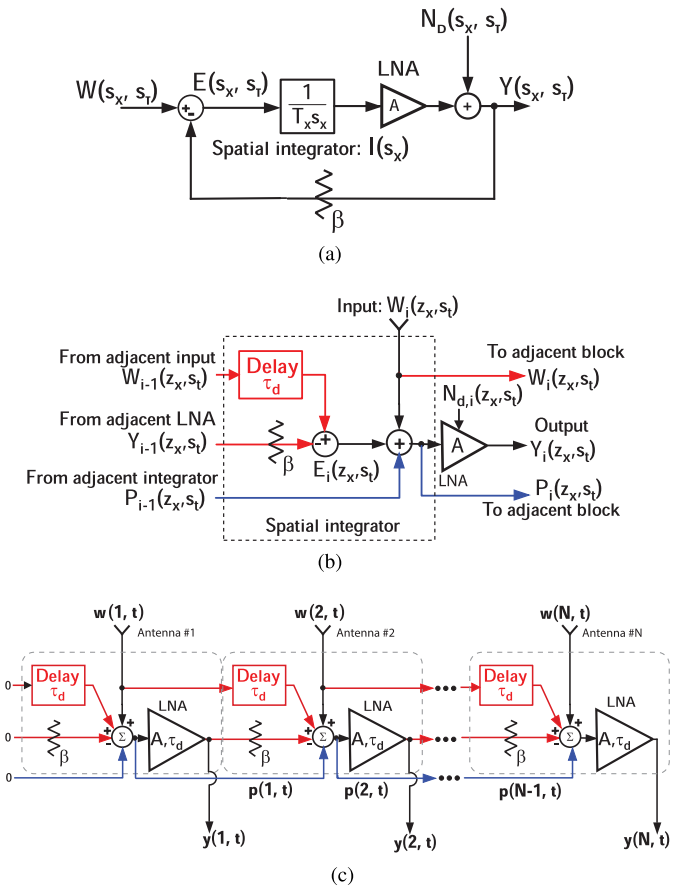

Fig. 5. Block diagram of the Δ-Σ Network. (a) Prototype network. (b) Spatial integrator followed by a gain where $P_{i\text{-}1}(z_x, s_t) \overset{\mathscr{L}}{\leftrightarrow} p_{i\text{-}1}(x, t)$, and (c) Δ-Σ network of the N-element sRx, where $e_i = w_{i\text{-}1} + \beta y_{i\text{-}1}$, $p_i = w_i + w_{i\text{-}1} - n_{d,i\text{-}1}\beta$, $y_i = A(w_i + w_{i\text{-}1}) + n_{d,i} - n_{d,i\text{-}1}$, and $A = 1/\beta$. Red lines: Rx chain interconnection paths. Blue lines: spatial-integrator outputs.

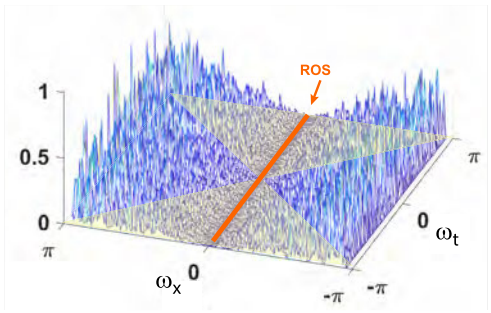

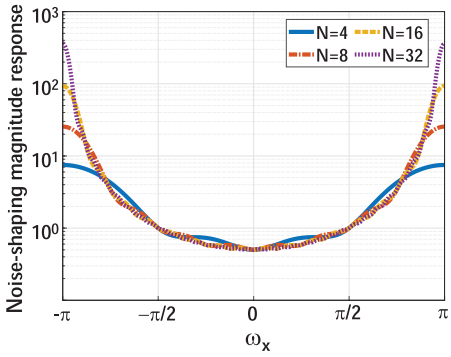

Fig. 6. (a) ST noise shaping for the ROS at $\omega_x = 0$ along the trough of the noise floor. The outline of the "light cone" is shown with a yellow shaded area. (b) Noise-shaping response as the function of the array size (N) vs spatial frequency when P interconnects are not implemented thus limiting gain to 1/2 at $\omega_x = 0$ instead of 0.

propagate to the adjacent chain, the adder cannot be merged with the LNA. Thus, in our demonstrator, we removed the P interconnections and accepted less than perfect behavior with respect to ND shaping, whereby the low spatial frequency gain of the ND-shaping filter increased to 1/2 from zero as illustrated in Fig. 6(b). Additionally, Fig. 6(b) also shows that the noise-shaping response is dependent on the size of the array. Placing building blocks in Fig. 5(b) (without the P adder at each antenna) and interconnecting adjacent blocks as in Fig. 5(c) yields the sRx demonstrator (sRx_demo) in Fig. 7, which includes pre-amplifiers LNA_1s, contains N outputs, and is constructed with *conventional* 2-port amplifiers, adders, attenuators, and "τ_d" delays that compensate for the LNA_2 group delay (τ_d). In sRx_demo, the LNA_2 and the gain stage ($M_{2,3}$) were used to represent an Rx in Fig. 4. The circuit diagram of the main components of this system are shown in Figs. 8 and 9.

Note that (14) and (16) ignore noise associated with the spatial integrator, which consists of the attenuator (β), time delay (τ_d), and summing junctions within each building block of the sRx. Since the NDs created by these components are not pushed to higher spatial frequencies, they limit the improvement to sensitivity of the sRx. Following the sRx stage, any spatial filter or beamforming (e.g., [23], [24]) can be used.

IV. Description of Main Circuits

Fig. 7 depicts the schematic of the sRx_demo, a 4-antenna sRx demonstrator, that was implemented in this work to demonstrate the viability of the ND-shaping concept. The key components comprising this circuit are described below.

A. Spatial Integrator

To implement the spatial integrator, we incorporate the integrator within a common-source stage ($M_{2,3}$) (shown in Fig. 7), wherein the SOI transistor M_3 is employed to feed the signal from an adjacent chain and antenna into the sRx_demo gain stages. By connecting $y_{i\text{-}1}$ to the back-gate of M_3, the attenuation β is implemented, where the size of M_3 is selected to provide the required attenuation via $g_{mb3} \approx 0.1 \times g_{m3}$ and to ensure the back-gate impedance does not affect the gain A of the LNA_2. Since the ratio between g_{mb3} and g_{m3} determines β, it also determines $A = \beta^{-1}$. In this design, M_2 and M_3 are sized to have the same g_m. The total width of M_2 is set to 23 μm with a gate-finger width of 0.5 μm, while the total width of M_3 is set to 29 μm with a gate-finger width of 0.5 μm. For $M_{2,3}$, the transistor multiplier is set to 1, and the vertical gate connection was set to 2. R_f is 3 kΩ. Simulations results of this circuit show gain between 1 and 3.3 dB, NF of 4.75 dB, P1dB of −14 dBm, and power consumption of 1.8 mW. To make signal subtraction possible, y_i needs to be

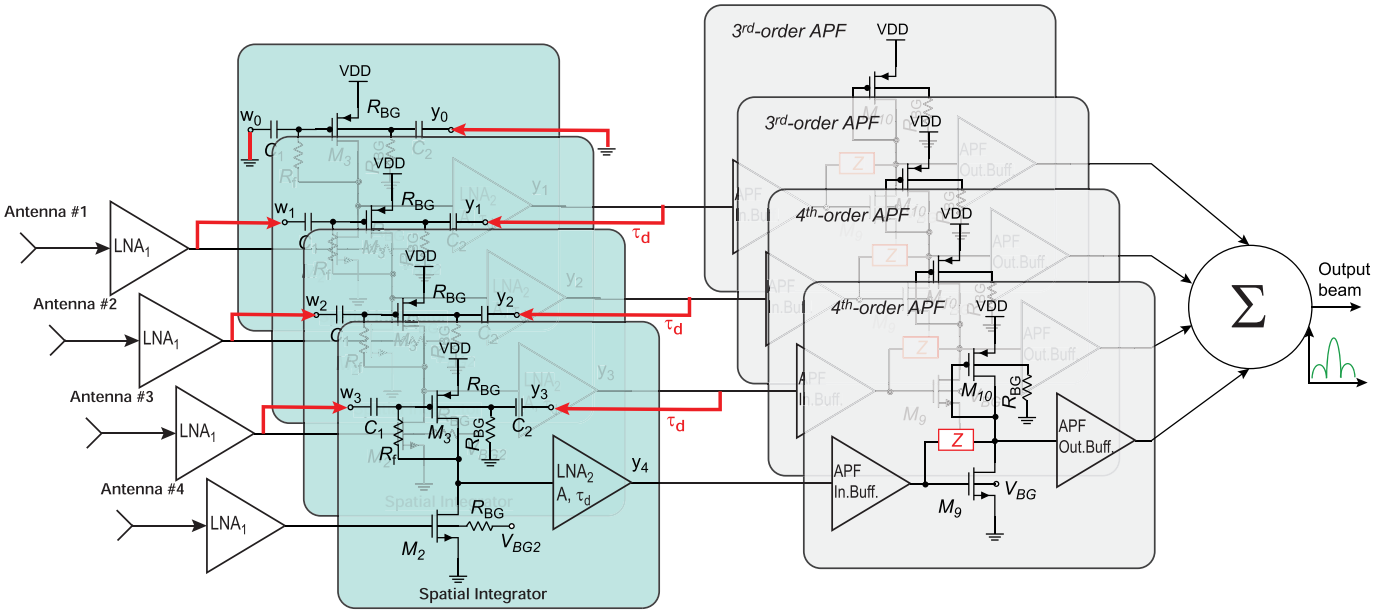

Fig. 7. Schematic of the sRx_demo. Back-gate terminals of the SOI process are used to reduce the transistor threshold voltages. The phase-distribution network brings the physically separated adder inputs to the same point on the chip. The red lines identify connections between the chains. A reference Rx (rRx) was implemented by removing C_1 and C_2 thereby removing interconnections between the four Rx chains.

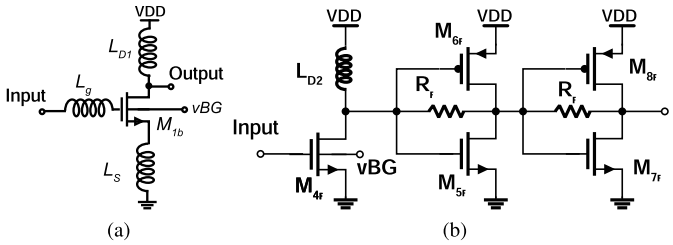

Fig. 8. Schematics of (a) LNA_1 and (b) LNA_2.

180° out of phase in relation to w_{i-1}. Therefore, the LNA_2 in Fig. 8(b) consists of three common-source stages. Post-layout simulations of the LNA_2 show NF between 4.7 and 5.7 dB, the gain between 18.3 and 21.5 dB, IP1dB between −14.7 and −11.3 dBm, and the power consumption of 4.25 mW. Delay $\tau_d \approx 35$ ps is created with a metal trace, which forms a connection with the adjacent chain and matches the group delay of the LNA_2 at 29 GHz as shown in Fig. 10.

B. Pre-Amplifier (LNA_1)

A low-power source-degenerated LNA_1 [Fig. 8(a)], consisting of M_{1b}, L_g, L_s, and L_{d1}, is included for ease of input impedance matching. The total width of M_{1b} is set to 34.5 μm with a gate finger width of 0.5 μm. The transistor multiplier is set to 1, and the vertical gate connection is set to 3. To reduce the minimum noise figure (NF) of the LNA_1, M_{1b} is biased at a current density of 150 μA/μm [25]. $L_g = 500$ pH is implemented with a wirebond, while $L_s = 50$ pH is implemented with a metal trace and a spiral inductor is used for $L_{d1} = 300$ pH. Although LNA_1 eases the implementation of the ND-shaping demonstrator, it is not necessary in future implementations of ND-shaping within array receivers. The LNA_1 cannot be measured on its own, but post-layout simulations, reported in Fig. 11, show an

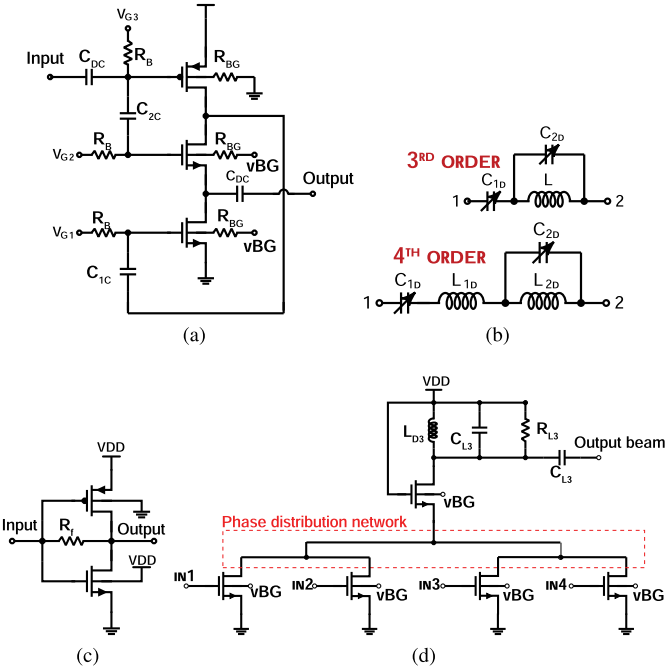

Fig. 9. Beamformer related schematics: (a) APF input buffer. (b) APF impedance networks. (c) APF output buffer. (d) Beamformer adder.

NF≈1.7 dB and gain (S_{21}) varying between 8.1 and 6.8 dB in the band of the sRx_demo operation while consuming 3.2 mW of power and exhibiting IP1dB between −12 and −10 dBm. The NDs of the LNA_1 are not shaped by the sRx_demo.

C. Beamformer

While most beamformers can be used here, a wideband delay-and-sum (DAS) beamformer (i.e., a spatial filter) is selected to filter out the receiver NDs that are shaped away from the desired ROS. Unlike often-used phase-and-sum

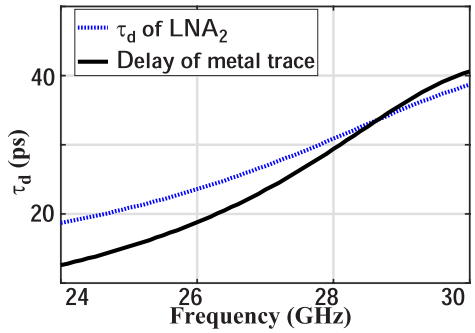

Fig. 10. Comparison of post-layout simulated LNA_2 τ_d and the delay realized with a metal trace used for interconnection adjacent chains.

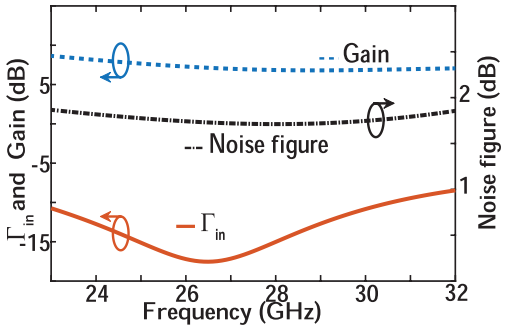

Fig. 11. Post-layout simulation results of the LNA_1 noise figure, input reflection coefficient, and gain.

beamformers, which employ phase shifters to compensate for DOA- and antenna-spacing-related and frequency-dependent phase differences experienced by temporally narrowband components of a PW as they reach the antennas in an array, a DAS beamformer compensates for propagation delays, which equally affect a wideband range of temporal components. Since the required delay difference in the desired band prescribes a certain delay-bandwidth product via the Padé approximation, the true-time-delay elements are implemented with third and fourth-order active all-pass filters (APFs) (Figs. 7 and 9) for long and short delays, respectively, to realize 0°, 22.5°, and 35° beams, where the APFs were designed to generate a delay difference of up to 27 ps to steer beams to 35° [26], [27]. The network "Z" in these figures realizes both poles and zeros in the transfer function, thereby halving the number of passive components needed for passive delay lines. The APF outputs are combined in an adder [Fig. 9(d)] that incorporates a symmetrical binary tree to preserve their amplitudes and phases.

A convenient property of these APFs is that their variable capacitors, C_{1d} and C_{2d} noted in Fig. 9(b), maintain the same ratio for different delays. This allows the adjustment of the network "Z" with one control voltage. Another voltage is applied to the back-gate of the SOI transistor M_9 in Fig. 7 to adjust its transconductance as required for maintaining the Padé delay approximation [27]. Post-layout simulations show that the cascade of APFs and input and output buffers exhibits the gain of −7 dB, NF of 9 dBm, IP1dB of −18 dBm, while consuming 7.4 mW of power. The adder consumes additional 12 mW, has the gain of −0.8 dB, NF of 7 dB, and IP1dB of −13 dBm.

In addition to the sRx_demo, a reference Rx (rRx) is also implemented. This rRx omits dc-blocking capacitors C_1 and

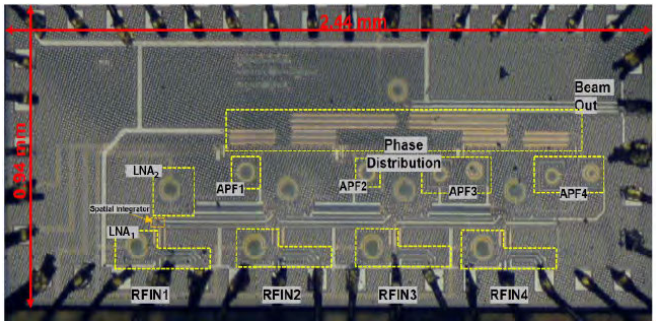

Fig. 12. Die micrograph.

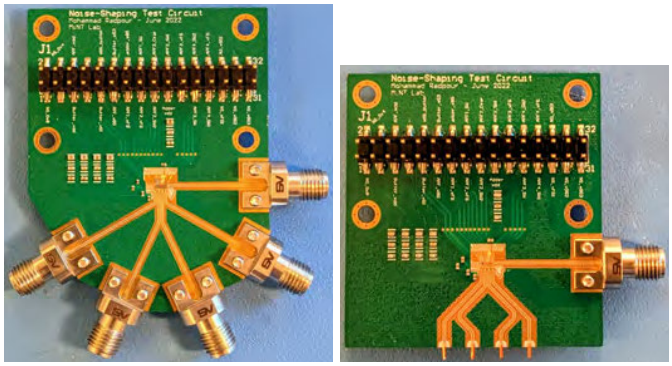

(a) (b)

Fig. 13. (a) Die on a test PCB for benchtop measurements. (b) Die wirebonded to a PCB with a 4-element array.

C_2 (see Fig. 7) to disable ND shaping (i.e., disconnecting the red lines) and realize the receiver as 4 independent receiver chains.

V. Measurement Results

The ND-shaping sRx_demo was implemented for a 4-element linear array. A photo of the 22-nm FDSOI-CMOS die with an active area of 1.6 mm^2 is shown in Fig. 12. The dice were mounted on custom-made PCBs in Fig. 13(a) for benchtop measurements and on a PCB in Fig. 13(b) for over-the-air measurements in an anechoic chamber.

The S-parameters, NFs, and linearity (IP1dB) of the sRx_demo and rRx were all measured using the same setup shown in Fig. 14.

The S-parameters and IP1dBs were measured using a Keysight P5008A vector network analyzer (VNA), which also measures NFs. Two preamplifiers (ERZIA's ERZ-LNA-0200-5000-22-6 and ERZ-HPA-1500-2700-29-E) were added at the VNA receiver port to improve the VNA sensitivity during NF measurements. IIP3s were measured with Keysight PNA-X network analyzer.

For over-the-air measurements, the dice were mounted on PCBs with 4-element antenna arrays [Fig. 13(b)] and placed in an anechoic chamber shown in Fig. 15(d) where the transmitter horn antenna was positioned 1-m away from the sRx_demo or rRx to measure beam patterns.

Beam patterns obtained at the lower (24.5 GHz), mid (26.5 GHz), and upper (28.5 GHz) band edges are shown in Fig. 15 (a)–(c). The measured S-parameters are shown in Fig. 16(a).

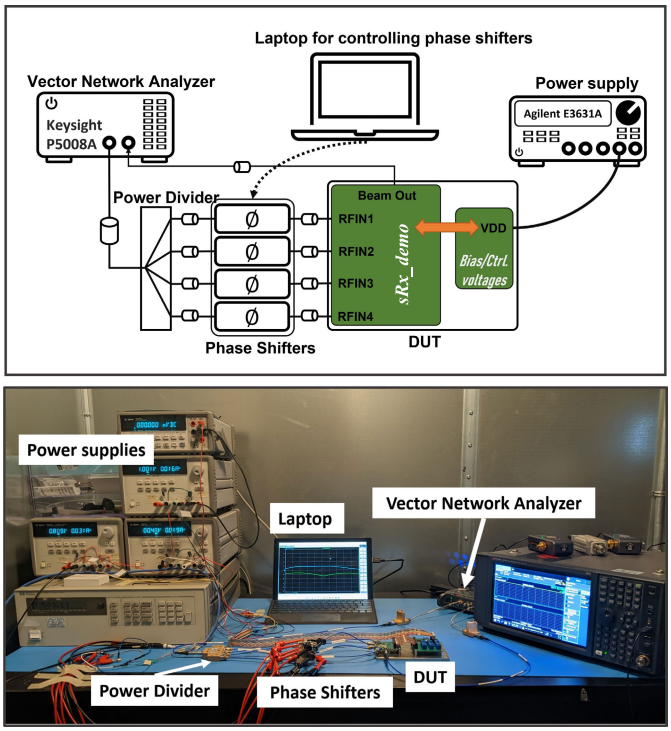

Fig. 14. Benchtop measurement setup.

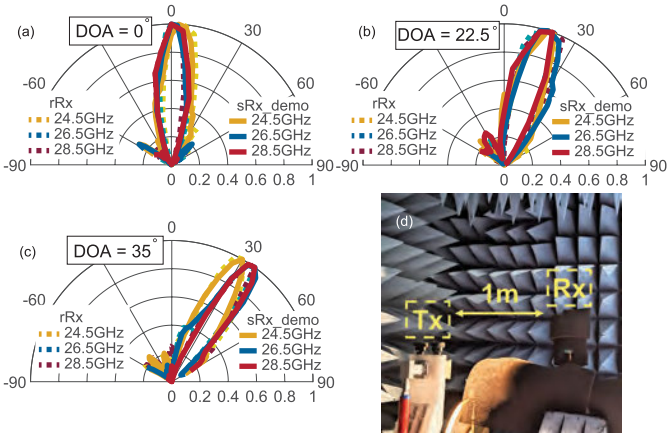

Fig. 15. Measured over-the-air beam patterns for low (24.5 GHz), mid (26.5 GHz), and high (28.5 GHz) frequencies are in (a) 0°, (b) 22.5°, and (c) 35°. (d) Over-the-air measurement setup in an anechoic chamber.

As can be seen, virtually identical S-parameter and beam measurements of the sRx_demo and rRx confirm their independence of ND shaping. Since it was not possible to determine noise and linearity via over-the-air measurements, the NF, IP1dB, and IIP3 for the sRx_demo and rRx [Figs. 15 (b) and (c)] were only measured for the 0° beam on the bench. The results show that the sRx_demo offered an average improvement of 2.25 dB in IP1dB, 1.6 dB in NF, and 1.4 dB in IIP3 compared to the rRx, even though the true improvements were somewhat obfuscated by the gain and linearity of the LNA_1 and the linearity of the beamformer. Nevertheless, these measured improvements agree with simulations and confirm the ND shaping by the sRx_demo. Furthermore, EVM measurement results reported in Fig. 16(d) also show improved ND behavior for sRx_demo.

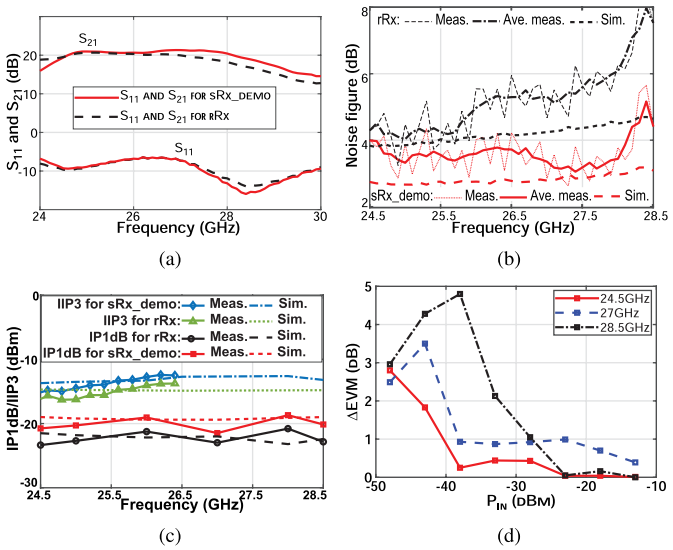

Fig. 16. Measured (a) S_{21} for the 0° beam of sRx_demo and rRx with the input applied via a power divider and S_{11} of individual sRx_demo and rRx signal chains, (b) NF, (c) IP1dB and IIP3 (1 MHz tone spacing), and (d) EVM improvement $\Delta\text{EVM} = \text{EVM}_{\text{rRx}} - \text{EVM}_{\text{sRx\_demo}}$, where EVM_{rRx} and $\text{EVM}_{\text{sRx\_demo}}$ are measured EVMs [dB] for rRx and sRx_demo, respectively. Measurements in (b)-(d) are for the 0° beam. The EVMs were measured with a 50MHz OFDM 64QAM modulation. In (a)–(c), the input power divider is de-embedded.

Measurements show a significant increase in NF of the rRx receiver at high temporal frequencies. The reason for this increase is not completely understood; however, the possible explanation for this increase is due to the small number of antennas used in the array. When there are only a few antennas (i.e., 4 in the case of rRx and sRx_demo), the ROS is no longer described by the Dirac delta function in (5) but rather by a sinc function, thereby spreading the ROS spatially. With the spatial sampling introducing a spatial aliasing of NDs into the spread ROS, there is a likelihood of the antenna array receiving additional noise at higher temporal frequencies. When ND-shaping is enabled, this aliasing is reduced as demonstrated by much improved NF of the sRx_demo circuit.

Table I summarizes the performance of our ND-shaping demonstrator and other receivers operating over similar frequency ranges. As can be seen, the rRx provides very competitive performance, which is further improved by enabling ND shaping in the sRx_demo.

The performance improvements exhibited by sRx_demo require circuits that otherwise are not needed in array receivers. For example, the gain stage $M_{2,3}$ of the sRx_demo is only added to provide the means of connecting adjacent chains to form a spatial integrator. This extra stage consumes 1.8 mW of power, occupies $12 \times 15\ \mu$m of area, and introduces some NDs. It is possible to avoid this active stage and instead use transformers for creating a spatial integrator that occupy a larger area [10]. However, the interconnections between adjacent chains may lead to instability concerns due to additional coupling between chains. This needs to be considered during the design stage. Regardless of how the spatial integrator is implemented, it consumes chip area and may consume extra power. These, however, are relatively minor overhead costs comparing for improving Rx sensitivity and linearity, as such

TABLE I
PERFORMANCE SUMMARY OF OUR ND-SHAPINGDEMONSTRATOR AND OTHER RECEIVERS

	This work		ISSCC	T-MTT	JSSC	CICC	ISSCC
	sRx_demo	**rRx**	2019 [24]	2020 [28]	2022 [29]	2021 [30]	2022 [23]
Frequency (GHz)	**24.3 to 28.7**		27 to 41	22 to 44	24 to 29.5	24 to 32	23 to 29
No. of Elements	**4**		4	1	4	4	4
Min. Noise Figure (dB)	**2.6**	**4**	4.3	3	4.3	4.3	4.8
Max. Gain (dB)	**21.3**	**20.7**	36	26.3	14.2	25.2	30
Max. IP1dB (dBm)	**-18.7**	**-20.8**	NR[b]	-24.5	-22.2	-23.1	-14[d]
Max. IIP3 (dBm)	**-12.5**	**-13.8**	–	–	-12.3[f]	–	–
P_{DC} per element (mW)	**19.8**[a]		70 to 85[c]	112	82	45	44.1[e]
Area (mm^2)	**2.3** **1.6 (core)**		23.4	4.5 1.89 (core)	34.32	6.84 1.21 (core)	2.8 2.08 (core)
Technology	**22nm SOI**		45nm SOI	45nm SOI	65nm CMOS	65nm CMOS	40nm CMOS

[a]the ND-shaping consumes 9.25 mW per element; [b]Not reported; [c]Includes mixers and LOs.
[d]in-notch IP1dB. [e]Includes mixers. [f] single-chain measurement.

improvements require receivers that consume more power than what is needed for a spatial integrator.

VI. CONCLUSION

This article reports the first demonstration of a novel approach to ST noise shaping in an antenna-array receiver. We implemented a Δ-Σ method in the spatial domain to move ND components originating in the receiver away from the ST ROS of incoming signals and toward the "Elsewhere" region located outside the "light cone" for removal by a beamformer. The demonstration was carried out using a 4-element linear antenna array and a custom-made 22-nm FDSOI CMOS chip, which achieved average improvements of 1.6, 1.4, and 2.25 dB in NF, IIP3, and IP1dB, respectively, over a reference design that also provides a very competitive performance. The sRx_demo shows that ND shaping is practical by exhibiting lower NF and higher IP1dB/IIP3 than rRx while having the same power consumption, gains, beam patterns, and areas.

ACKNOWLEDGMENT

The authors thank the Global Foundries for providing silicon fabrication through the 22FDX university program. They also would like to acknowledge CMC Microsystems and Canada's National Design Network (CNDN) for the provision of Cadence, Keysight ADS, and Altium Designer that facilitated this research.

REFERENCES

[1] E. Brookner, "Never ending saga of phased array breakthroughs," in *Proc. IEEE Int. Symp. Phased Array Syst. Technol.*, Oct. 2010, pp. 61–73.

[2] B. D. Van Veen and K. M. Buckley, "Beamforming: A versatile approach to spatial filtering," *IEEE ASSP Mag.*, vol. 5, no. 2, pp. 4–24, Apr. 1988.

[3] W. Roh et al., "Millimeter-wave beamforming as an enabling technology for 5G cellular communications: Theoretical feasibility and prototype results," *IEEE Commun. Mag.*, vol. 52, no. 2, pp. 106–113, Feb. 2014.

[4] S. Mondal, R. Singh, A. I. Hussein, and J. Paramesh, "A 25-30 GHz 8-antenna 2-stream hybrid beamforming receiver for MIMO communication," in *Proc. IEEE Radio Freq. Integr. Circuits Symp. (RFIC)*, Jun. 2017, pp. 112–115.

[5] S. Dutta, C. N. Barati, D. Ramirez, A. Dhananjay, J. F. Buckwalter, and S. Rangan, "A case for digital beamforming at mmWave," *IEEE Trans. Wireless Commun.*, vol. 19, no. 2, pp. 756–770, Feb. 2020.

[6] J. D. Dunworth et al., "A 28 GHz bulk-CMOS dual-polarization phased-array transceiver with 24 channels for 5G user and basestation equipment," in *IEEE Int. Solid-State Circuits Conf. (ISSCC) Dig. Tech. Papers*, Feb. 2018, pp. 70–72.

[7] N. Liyanage, L. Bruton, and P. Agathoklis, "On the attenuation of interference and mutual coupling in antenna arrays using 3D space-time filters," in *Proc. IEEE Pacific Rim Conf. Commun., Comput. Signal Process.*, Aug. 2009, pp. 146–151.

[8] L. Larson, T. Cataltepe, and G. Temes, "Multibit oversampled Σ-Δ A/D convertor with digital error correction," *Electr. Lett.*, vol. 24, no. 16, pp. 1051–1052, 1988.

[9] T. S. Rappaport et al., "Wireless communications and applications above 100 GHz: Opportunities and challenges for 6G and beyond," *IEEE Access*, vol. 7, pp. 78729–78757, 2019.

[10] Y. Wang, S. Handagala, A. Madanayake, L. Belostotski, and S. Mandal, "N-port LNAs for mmW array processors using 2-D spatio-temporal $\Delta - \Sigma$ noise-shaping," in *Proc. IEEE 60th Int. Midwest Symp. Circuits Syst. (MWSCAS)*, Aug. 2017, pp. 1473–1476.

[11] L. Bruton and N. Bartley, "Three-dimensional image processing using the concept of network resonance," *IEEE Trans. Circuits Syst.*, vol. CS-32, no. 7, pp. 664–672, Jul. 1985.

[12] R. Ansari, "Efficient IIR and FIR fan filters," *IEEE Trans. Circuits Syst.*, vol. CS-34, no. 8, pp. 941–945, Aug. 1987.

[13] L. Khademi and L. T. Bruton, "Reducing the computational complexity of narrowband 2D fan filters using shaped 2D window functions," in *Proc. Int. Symp. Circuits Syst. (ISCAS)*, Mar. 2003, pp. 702–705.

[14] C. Wijenayake, Y. Xu, A. Madanayake, L. Belostotski, and L. T. Bruton, "RF analog beamforming fan filters using CMOS all-pass time delay approximations," *IEEE Trans. Circuits Syst. I, Reg. Papers*, vol. 59, no. 5, pp. 1061–1073, May 2012.

[15] Y. Naya, K. Ichige, and H. Arai, "Design of 2-D FIR fan filters for wideband beamforming and interference suppression," in *Proc. Eur. Radar Conf. (EuRAD)*, Sep. 2009, pp. 425–428.

[16] C. Wijenayake, A. Madanayake, L. Belostotski, Y. Xu, and L. Bruton, "All-pass filter-based 2-D IIR filter-enhanced beamformers for AESA receivers," *IEEE Trans. Circuits Syst. I, Reg. Papers*, vol. 61, no. 5, pp. 1331–1342, May 2014.

[17] C. U. S. Edussooriya, L. T. Bruton, P. Agathoklis, and T. K. Gunaratne, "Low-complexity maximally-decimated multirate 3-D spatio-temporal FIR cone and frustum filters," *IEEE Trans. Circuits Syst. I, Reg. Papers*, vol. 60, no. 7, pp. 1845–1856, Jul. 2013.

[18] A. Madanayake, C. Wijenayake, and L. Belostotski, "Continuous-time 2-D IIR+time-delay linear aperture arrays," in *Proc. IEEE Radio Wireless Symp. (RWS)*, Jan. 2015, pp. 38–40.

[19] H. Malavipathirana et al., "Spatio-temporal Δ-Σ N^2-port ADC noise shaping for N×N antenna arrays," in *Proc. IEEE Int. Symp. Circuits Syst.*, Sep. 2020, pp. 1–5.

[20] H. L. Van Trees, *Optimum Array Processing. Detection, Estimation, and Modulation Theory*. Hoboken, NJ, USA: Wiley, 2004.

[21] L. T. Bruton, A. Madanayake, C. Wijenayake, and M. Maini, "Continuous-time analog two-dimensional IIR beam filters," *IEEE Trans. Circuits Syst. II, Exp. Briefs*, vol. 59, no. 7, pp. 419–423, Jul. 2012.

[22] L. Bruton and N. Bartley, "Highly selective three-dimensional recursive beam filters using intersecting resonant planes," *IEEE Trans. Circuits Syst.*, vol. CS-30, no. 3, pp. 190–193, Mar. 1983.
[23] L. Zhang and M. Babaie, "A 23-to-29 GHz receiver with mm-wave N-input-N-output spatial notch filtering and autonomous notch-steering achieving 20-to-40dB mm-wave spatial rejection and -14dBm in-notch IP1 dB," in *IEEE Int. Solid-State Circuits Conf. (ISSCC) Dig. Tech. Papers*, Feb. 2022, pp. 82–84.
[24] M.-Y. Huang and H. Wang, "A 27-to-41 GHz MIMO receiver with N-input-N-output using scalable cascadable autonomous array-based high-order spatial filters for instinctual full-FoV multi-blocker/signal management," in *IEEE Int. Solid-State Circuits Conf. (ISSCC) Dig. Tech. Papers*, Feb. 2019, pp. 346–348.
[25] T. O. Dickson et al., "The invariance of characteristic current densities in nanoscale MOSFETs and its impact on algorithmic design methodologies and design porting of Si(Ge) (Bi)CMOS high-speed building blocks," *IEEE J. Solid-State Circuits*, vol. 41, no. 8, pp. 1830–1845, Aug. 2006.
[26] Z. Kabirkhoo, M. Radpour, and L. Belostotski, "Wideband high-order all-pass delay circuits," in *Proc. 19th IEEE Int. New Circuits Syst. Conf. (NEWCAS)*, Jun. 2021, pp. 1–4.
[27] Z. Kabirkhoo, M. Radpour, and L. Belostotski, "Tunable wideband high-order active analog delays with high delay-bandwidth product," *IEEE Microw. Wireless Technol. Lett.*, vol. 33, no. 8, pp. 1203–1206, Sep. 2023.
[28] L. Gao and G. M. Rebeiz, "A 22–44-GHz phased-array receive beamformer in 45-nm CMOS SOI for 5G applications with 3–3.6-dB NF," *IEEE Trans. Microw. Theory Techn.*, vol. 68, no. 11, pp. 4765–4774, Nov. 2020.
[29] Y. Yi et al., "A 24–29.5-GHz highly linear phased-array transceiver front-end in 65-nm CMOS supporting 800-MHz 64-QAM and 400-MHz 256-QAM for 5G new radio," *IEEE J. Solid-State Circuits*, vol. 57, no. 9, pp. 2702–2718, Sep. 2022.
[30] W. Zhu, J. Wang, R. Wang, and Y. Wang, "A dual-mode 24-32 GHz 4-element phased-array transceiver front-end with SSA beamformer for autonomous agile unknown signal tracking and blocker rejection within <0.1 us and 21.3%/15% transmitter Peak/OP1dB PAE," in *Proc. IEEE Custom Integr. Circuits Conf. (CICC)*, Apr. 2021, pp. 1–2.

Mohammad Radpour (Member, IEEE) received the B.Sc. and M.Sc. degrees in electrical and computer engineering from the Isfahan University of Technology, Isfahan, Esfahan, Iran, in 2013 and 2016, respectively, and the Ph.D. degree in electrical and electronics engineering from the Department of Electrical and Software Engineering, University of Calgary, Calgary, AB, Canada, in 2023.

He is currently a Lead Design Engineer at Cadence Design Systems. His research interests include the design of analog integrated circuits, as well as RF/mm-wave circuits and systems such as low-noise amplifiers, all-pass filters, and beamformers.

Dr. Radpour is a Member of IEEE Young Professionals and a Member of IEEE Solid-State Circuits Society.

Zahra Kabirkhoo (Member, IEEE) received the dual B.Sc. degree (Hons.) in electrical engineering and biomedical engineering and the M.Sc. degree in biomedical engineering from Amirkabir University, Tehran, Iran, in 2016 and 2018, respectively. She is currently pursuing the Ph.D. degree in electrical engineering at the University of Calgary, Calgary, AB, Canada.

Her current research interests include mixed-signal integrated circuits with a focus on high-speed ADCs.

Ms. Kabirkhoo is a Member of IEEE Solid-States Circuits Society.

Arjuna Madanayake (Member, IEEE) received the B.Sc. (Eng.) degree (Hons.) in electronic and telecommunication engineering from the University of Moratuwa, Moratuwa, Sri Lanka, in 2002, and the M.Sc. and Ph.D. degrees in electrical engineering from the University of Calgary, Calgary, AB, Canada, in 2004 and 2008, respectively.

He is an Associate Professor with the Department of Electrical and Computer Engineering (ECE), Florida International University (FIU), Miami, FL, USA. He leads the RF, Analog and Digital (RAND) Lab for Advanced Signal Processing Circuits (ASPC), where his research has been recently supported by multiple grants from NSF, ONR, NASA, NIH, and DARPA. His research interests include spanning signal processing, wireless communications, analog and digital circuits, RF systems, antenna arrays, FPGA systems, radar and electronic warfare, fast algorithms and VLSI, analog computing, radio astronomy instrumentation, 5G/6G mm-wave systems, advanced spectrum, blockchain applications for spectrum, RF-machine learning, AI accelerators for 6G, and software defined radio (SDR).

Soumyajit Mandal (Senior Member, IEEE) received the B.Tech. degree from the Indian Institute of Technology (IIT) Kharagpur, Kharagpur, India, in 2002, and the S.M. and Ph.D. degrees in electrical engineering from the Massachusetts Institute of Technology (MIT), Cambridge, MA, USA, in 2004 and 2009, respectively.

He was a Research Scientist with Schlumberger-Doll Research, Cambridge, from 2010 to 2014, an Assistant Professor with the Department of Electrical Engineering and Computer Science, Case Western Reserve University, Cleveland, OH, USA, from 2014 to 2019, and an Associate Professor with the Department of Electrical and Computer Engineering, University of Florida, Gainesville, FL, USA, from 2019 to 2021. He is currently a Senior Engineer with the Instrumentation Division, Brookhaven National Laboratory, Upton, NY, USA. He has over 150 publications in peer-reviewed journals and conferences and has been awarded 26 patents. His research interests include analog and biological computation, magnetic resonance sensors, low-power analog and RF circuits, and precision instrumentation for various biomedical and sensor interface applications.

Dr. Mandal was a recipient of the President of India Gold Medal in 2002, the MIT Microsystems Technology Laboratories (MTL) Doctoral Dissertation Award in 2009, the T. Keith Glennan Fellowship in 2016, and the IIT Kharagpur Young Alumni Achiever Award in 2018.

Leonid Belostotski (Senior Member, IEEE) received the B.Sc. and M.Sc. degrees in electrical engineering from the University of Alberta, Edmonton, AB, Canada, in 1997 and 2000, respectively, and the Ph.D. degree from the University of Calgary, Calgary, AB, Canada, in 2007. He was a RF Engineer with Murandi Communications Ltd., Calgary, from 2001 to 2004. He is currently a Professor with the University of Calgary and the Canada Research Chair in high-sensitivity radiometers and receivers. His current research interests include RF and mixed-signal ICs, high-sensitivity receiver systems, antenna arrays, and terahertz systems.

Mr. Belostotski was a recipient of the Outstanding Student Designer Award from Analog Devices Inc., in 2007, and the IEEE Microwave Theory and Techniques-11 Contest on Creativity and Originality in Microwave Measurements, in 2008. He serves as the IEEE SOUTHERN ALBERTA SOLID-STATE, CIRCUITS AND CIRCUITS AND SYSTEMS CHAPTER'S CHAIR. He served as an Associate Editor for the IEEE TRANSACTIONS ON INSTRUMENTATION AND MEASUREMENT. He is the Editor-in-Chief for the *IEEE Solid-State Circuits Magazine*.